Nanoscale

PAPER

Check for updates

Cite this: *Nanoscale*, 2023, **15**, 19546

Core–multi-shell design: unlocking multimodal capabilities in lanthanide-based nanoparticles as upconverting, T_2-weighted MRI and CT probes†

Nan Liu, [ID] [a] Christian Homann, [ID] [a] Samuel Morfin,[b] Meghana S. Kesanakurti,[a] Nicholas D. Calvert,[a,c] Adam J. Shuhendler, [ID] [a,c,d] Tom Al[b] and Eva Hemmer [ID] *[a]

Multimodal bioimaging probes merging optical imaging, magnetic resonance imaging (MRI), and X-ray computed tomography (CT) capabilities have attracted considerable attention due to their potential biomedical applications. Lanthanide-based nanoparticles are promising candidates for multimodal imaging because of their optical, magnetic and X-ray attenuation properties. We prepared a set of hexagonal-phase (β)-$NaGdF_4$:Yb,Er/$NaGdF_4$/$NaDyF_4$ core/shell/shell nanoparticles (Dy-CSS NPs) and demonstrated their optical/T_2-weighted MRI/CT multimodal capabilities. A known drawback of multimodal probes that merge the upconverting Er^{3+}/Yb^{3+} ion pair with magnetic Dy^{3+} ions for T_2-weighted MRI is the loss of upconversion (UC) emission due to Dy^{3+} poisoning. Particular attention was paid to controlled nanoparticle architectures with tuned inner shell thicknesses separating Dy^{3+} and Er^{3+}/Yb^{3+} to shed light on the distance-dependent loss of UC due to $Yb^{3+} \rightarrow Dy^{3+}$ energy transfer. Based on the Er^{3+} UC spectra and the excited state lifetime of Yb^{3+}, a 4 nm thick $NaGdF_4$ inner shell did not only restore but enhanced the UC emission. We further investigated the effect of the outer $NaDyF_4$ shell thickness on the particles' magnetic and CT performance. MRI T_2 relaxivity measurements *in vitro* at a magnetic field of 7 T performed on citrate-capped Dy-CSS NPs revealed that NPs with the thickest outer shell thickness (4 nm) exhibited the highest r_2 value, with a superior T_2 contrast effect compared to commercial iron oxide and other Dy-based T_2 contrast agents. In addition, the citrate-capped Dy-CSS NPs were demonstrated suitable for CT in *in vitro* imaging phantoms at X-ray energies of 110 keV, rendering them interesting alternatives to clinically used iodine-based agents that operate at lower energies.

Introduction

Biomedical imaging plays a critical role in health and life sciences, from basic research to diagnostics and treatment.[1,2] Among the various imaging techniques currently available to healthcare providers and researchers, optical imaging allows for the investigation of time-dependent biological phenomena with high spatial imaging resolution and sensitivity. Yet, one

[a]*Department of Chemistry and Biomolecular Sciences, University of Ottawa, Ottawa, ON, Canada. E-mail: ehemmer@uottawa.ca*
[b]*Department of Earth and Environmental Sciences, University of Ottawa, Ottawa, ON, Canada*
[c]*University of Ottawa Heart Institute, Ottawa, ON, Canada*
[d]*Department of Biology, University of Ottawa, Ottawa, ON, Canada*

†Electronic supplementary information (ESI) available: Additional experimental details, including shell thickness control; additional structural analysis by XRD and TEM; additional optical characterization of OA-capped NPs; characterization of citrate-capped Dy-CSS NPs; nanothermometry of Cit-Dy-CSS NPs; MRI T_1 relaxivity measurements; X-ray spectroscopy and radiography imaging measurements. See DOI: https://doi.org/10.1039/d3nr05380f

of its major drawbacks is the low penetration depth of light.[3] In contrast, magnetic resonance imaging (MRI) and X-ray computed tomography (CT) imaging come with the advantage to provide physiological and anatomical information with unlimited penetration depth. However, their relatively low spatial resolution and sensitivity remain a challenge.[4] Merging the advantages of each imaging technique on its own, multimodal approaches have been proposed. In this vein, multifunctional nanoparticles (NPs) exhibiting properties suitable for two or more imaging modalities bear great potential as bioprobes enabling multimodal imaging.[5–10] These multimodal imaging probes may provide more precise diagnosis and monitoring of disease progression through integrating several imaging modalities with different properties into one nanoparticle platform.[11]

Lanthanide (Ln)-based materials are promising candidates for multimodal imaging probes because of their optical, magnetic, and X-ray attenuation properties.[6,7,12,13] Ln-based materials exhibit unique optical properties due to their capability to emit UV and visible light (upconversion) as well as

near-infrared (NIR) light (downshifting) when excited with NIR light (*e.g.* 980 or 808 nm).[14–16] Compared to conventional optical probes excited with UV-visible light, the use of NIR light provides several advantages, such as deeper penetration depth, weak autofluorescence, minimal photobleaching, and low phototoxicity.[16,17] In addition, gadolinium- (Gd^{3+}) and dysprosium- (Dy^{3+}) based materials have attracted growing attention as MRI contrast agents (CAs) because of their characteristic magnetic properties. Owing to the Gd^{3+} $4f^7$ electron configuration, Gd^{3+}-based chelates are commonly used as MRI T_1 CAs.[18,19] Gd^{3+}-based NPs have also been widely investigated as alternatives to chelates due to their longer blood circulation time and large density of Gd^{3+} ions on their surface, which dramatically increases the concentration of the contrast-providing species in the region of interest.[20–23] On the other hand, clinically used MRI T_2 CAs are based on iron oxides, which, however, suffer from magnetization saturation at high magnetic fields (greater than 3 T).[24] Dy^{3+} is a suitable candidate for high-field T_2 CAs due to its relatively large magnetic moment ($10.6\mu_B$) and short relaxation time, without saturation of the magnetization even at high magnetic fields up to 11.7 T.[25–28] High-field MRI is gaining increasing attention due to its higher spatial resolution and signal-to-noise ratio, holding potential for more effective diagnostic imaging.[28,29] Therewith comes the raising demand for suitable high-field T_2 CAs.

Ln-based NPs as optical/T_1 imaging probes combining luminescent Ln^{3+} (*e.g.* Er^{3+}, Tm^{3+}, Nd^{3+}, Ho^{3+}) and magnetic Gd^{3+} ions have been widely studied.[7,30–32] However, there are only a few reports about multimodal probes that combine optical and T_2 imaging capabilities.[5,6,9,33] A main reason for the slow development of optical/T_2 probes based on Ln^{3+} ions may be the severe quenching effect of Dy^{3+} on the UC luminescence, thus, hampering the probe's optical performance.[34] In order to circumvent the UC poisoning effect of Dy^{3+} ions, some studies suggested to physically separate Dy^{3+} from the luminescent Ln^{3+} ions, *e.g.* Er^{3+} or Tm^{3+}.[5,9,33–35] For instance, Su *et al.* synthesized $NaGdF_4$:Yb,Er/$NaDyF_4$ core/shell (CS) NPs and found that the UC emission intensity of Er^{3+} decreased upon shelling with $NaDyF_4$ because of the quenching effect of the Dy^{3+} ions.[34] To overcome this issue, Biju *et al.* proposed a strategy based on a lower Dy^{3+} concentration in the shell by preparing $NaGdF_4$:Yb,Er/$NaYbF_4$:Dy NPs with 38 mol% Dy^{3+} doped into the shell. While UC emission could be partially restored, the emission intensity still dropped by 27% compared to that of CS NPs with an undoped $NaGdF_4$ shell.[33] Moreover, reducing the amount of Dy^{3+} ions might not be advantageous when aiming for additional T_2 imaging capabilities. The introduction of an intermediate CaF_2 shell as a separating barrier between Dy^{3+} and the emitting Ln^{3+} ions was introduced by Li *et al.* A 2.3 nm thick inert shell between the upconverting Tm^{3+} ions in the core and the Dy^{3+} ions in the outer shell ($NaYbF_4$:Tm/CaF_2/$NaDyF_4$ core/shell/shell (CSS) architecture) allowed for UC emission intensities of Tm^{3+} as high as those from $NaYbF_4$:Tm/CaF_2 CS NPs.[5] This and related work demonstrated the high promise of the CSS architecture

design as a strategy towards optical/T_2-weighted MRI probes based on upconverting Ln^{3+} and Dy^{3+} ions.[6]

In addition, the potential of Ln-based NPs as CAs for CT imaging applications has been demonstrated,[36] given their relatively higher X-ray attenuation coefficients compared to clinically used iodine-based CAs (I: 1.9, Gd: 3.1, Dy: 3.4, Yb: 3.9 cm^2 g^{-1} at 100 keV[37]). The higher X-ray attenuation coefficient of these Ln-based NPs can confer higher efficacy than that of iodine-based CAs, thus, expecting to provide an equivalent contrast at a lower dose compared to the iodine-based CAs. This reduced dose requirement is highly beneficial in a contrast agent as it may reduce potential adverse effects in patients in clinical applications.[10,38]

The overarching goal of this work was to design Ln^{3+}-based nanoparticle probes that merge the manifold properties of the Ln^{3+} ions into one multimodal imaging agent that has UC, T_2-modulating, and CT capabilities. Inspired by previous work, here, we designed a set of CSS NPs, *i.e.*, hexagonal (β)-phase $NaGdF_4$:Yb,Er/$NaGdF_4$/$NaDyF_4$ (Dy-CSS, Fig. 1A). Particular attention was paid to the establishment of new protocols for the controlled shell growth *via* a rapid and straightforward microwave-assisted route. The adjustment of the inner and outer shell thicknesses allowed to (i) shed light on distance-dependent Dy^{3+} quenching effects and energy transfer mechanisms as well as (ii) assess the effect of shell thickness on T_2 MRI and CT performance. As a result, Dy-CSS NPs were obtained with not only restored but enhanced UC emission as well as superior T_2 and CT capabilities compared to previously reported nanoparticle architectures and common CAs, holding potential as a multimodal imaging probe.

Results and discussion

Synthesis and structural characterization of Dy-CSS NPs

A set of oleate (OA)-capped Dy-CSS NPs was successfully synthesized using a modified version of the microwave-assisted protocol previously established by our group.[21,39] Control over the shell thickness in multi-shell Ln-NPs is crucial to optimize their performance and to understand structure–property relationships. While the microwave-assisted route was previously reported as suitable for simple core/shell architectures, stringent control over shell thicknesses and the synthesis of core/multi-shell systems remained a challenge. Here, we demonstrate that the adjustment of the ratio between core NPs acting as seeds for shell growth and shell precursor (Gd-TFA) in the reaction mixture allowed to tune the thickness of the undoped $NaGdF_4$ shell on the Er/Yb-co-doped core from *ca.* 3 to 4 and 6 nm, respectively (Fig. 1, Fig. S1 and Table S1†). Following the same strategy, the thickness of the outer $NaDyF_4$ shell of the CSS Dy-NPs could be controlled (*vide infra*). A detailed description of the synthesis of the CSS NPs – hereafter labelled as ^{3nm}Dy-CSS^{3nm}, ^{4nm}Dy-CSS^{3nm}, and ^{6nm}Dy-CSS^{3nm}, whereas the first and second superscript indicate the thickness of the inner and outer shell, respectively – is provided in the Experimental section. X-ray diffraction (XRD) analysis confirmed that all the Dy-CSS NPs were of pure hexagonal phase
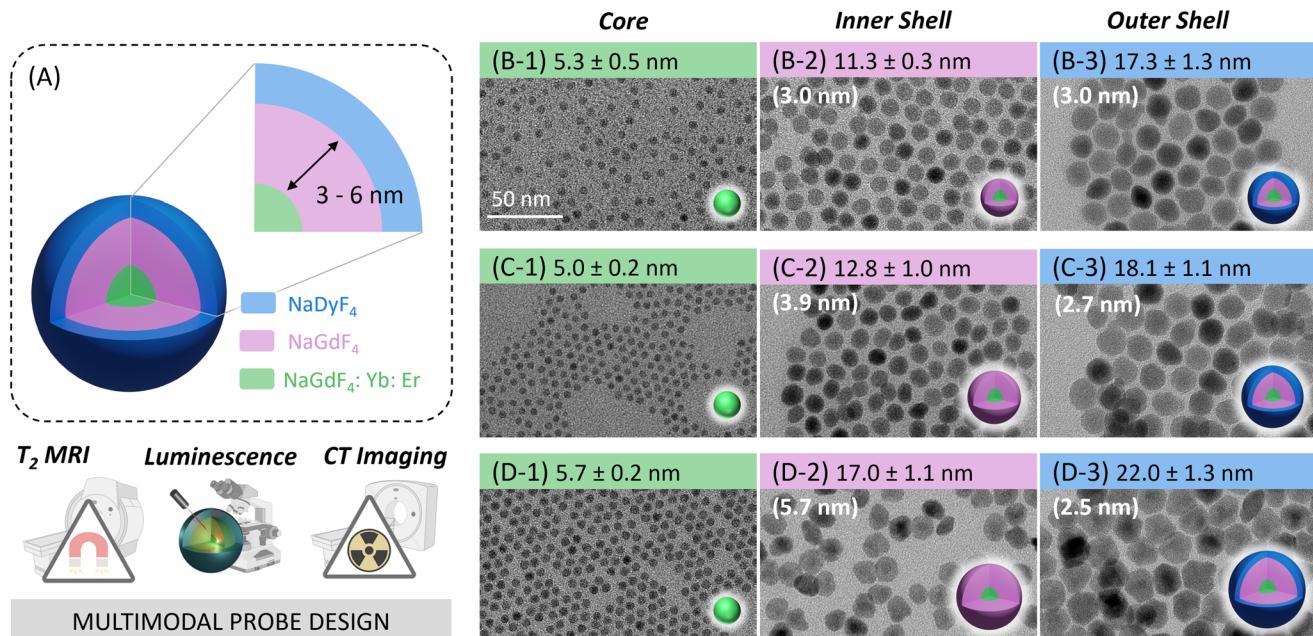
Fig. 1 (A) Schematic illustration of the core/shell/shell Dy-NP architecture proposed as multimodal optical/T_2/CT probe. (B–D) TEM images and sizes of OA-capped (1) core β-NaGdF$_4$:Yb,Er, (2) core/shell β-NaGdF$_4$:Yb,Er/NaGdF$_4$, and (3) core/shell/shell β-NaGdF$_4$:Yb,Er/NaGdF$_4$/NaDyF$_4$ NPs. The NaGdF$_4$ inner shell thickness and NaDyF$_4$ outer shell thickness are indicated in brackets. Core sizes and outer shell thicknesses were kept comparable, while the thickness of the inner shell increased from (B) to (D). The 50 nm scale bar applies to all TEM images.

of NaGdF$_4$ and NaDyF$_4$ (Fig. S2†). The morphology and size of core, CS and CSS NPs were examined by transmission electron microscopy (TEM). As shown in Fig. 1B–D and Fig. S3,† all NPs were monodisperse with narrow size distributions. The obtained NaGdF$_4$ core NPs, co-doped with 2 mol% Er^{3+} and 20 mol% Yb^{3+} to induce luminescent properties, exhibited a spherical morphology with an average diameter of *ca.* 5.4 nm. Growing an undoped NaGdF$_4$ shell resulted in CS NPs of 11.3 ± 0.3 nm, 12.8 ± 1.0 nm, and 17.0 ± 1.1 nm, with controlled shell thicknesses of *ca.* 3, 4, and 6 nm. Further growth of a *ca.* 2.7 nm thick NaDyF$_4$ outer shell to introduce Dy^{3+} ions for T_2-weighted MRI led to overall NP sizes of 17.3 ± 1.3 nm, 18.1 ± 1.1 nm, and 22.0 ± 1.3 nm for ^{3nm}Dy-CSS^{3nm}, ^{4nm}Dy-CSS^{3nm}, and ^{6nm}Dy-CSS^{3nm}, respectively. Importantly, the core size and outer shell thickness of the obtained Dy-CSS NPs were kept comparable among the three NP architectures, while three different inner shell thicknesses were introduced. Such control of the CSS architecture allows for the investigation of the efficiency of the inner barrier layer between the Er^{3+}/Yb^{3+} ions in the core and the Dy^{3+} ions in the outer shell.

Optical properties of Dy-CSS NPs

The upconversion (UC) luminescence properties of the obtained NPs, dispersed in toluene, were investigated under 980 nm excitation. As shown in Fig. 2(A-1), the emission spectra of ^{3nm}Dy-CSS^{3nm} and their corresponding core/shell (^{3nm}CS) and core NPs exhibited characteristic upconversion emission peaks in the green and red spectral regions ascribed to the $^2H_{11/2} \rightarrow ^4I_{15/2}$ (520 nm), $^4S_{3/2} \rightarrow ^4I_{15/2}$ (540 nm), and $^4F_{9/2} \rightarrow ^4I_{15/2}$ (650 nm) Er^{3+} transitions. The low emission

intensity obtained from core NPs was no surprise given the very small NP size (*ca.* 5 nm) resulting in severe surface quenching. When adding a 3 nm undoped NaGdF$_4$ shell, as expected, the emission intensity increased, reducing surface quenching effects.[40] However, the addition of an additional outer NaDyF$_4$ shell (^{3nm}Dy-CSS^{3nm} NPs) resulted in lower UC emission intensities than obtained for ^{3nm}CS NPs without the NaDyF$_4$. The observed loss (*ca.* 50% for both the green and red emissions) indicated that an inner shell of 3 nm thickness was not sufficient to protect the emitter pair Er^{3+}/Yb^{3+} from the Dy^{3+} quencher. Previous studies reported that an inner CaF$_2$ shell as thin as 2.3 nm was suitable to restore the UC emission,[5] while in our study, emission loss was observed with a 3 nm inner NaGdF$_4$ shell. This might be explained by potential cation intermixing in the Dy-CSS NPs taking place during shell growth, resulting in the distribution of Ln^{3+} dopant ions (*i.e.*, Er^{3+} and Dy^{3+}) into the nominally undoped shell.[40,41] As expected, growing a thicker inner shell of 4 nm on core NPs significantly increased the UC emission intensity, ^{4nm}CS NPs showing an overall 2000 times higher UC intensity than core NPs (Fig. 2(A-2)). Most interestingly, no loss of UC was observed upon the addition of an outer NaDyF$_4$ shell. The obtained ^{4nm}Dy-CSS^{3nm} NPs exhibited not only restored UC emission but an UC enhancement by more than 100% for the green and by *ca.* 270% for the red emission compared to their respective ^{4nm}CS NPs. This result indicated that an inner NaGdF$_4$ shell of at least 4 nm in thickness was required to overcome the Dy^{3+}-induced loss of UC.

Possible quenching processes caused by Dy^{3+} were previously proposed by Zhang *et al.* based on steady-state UC
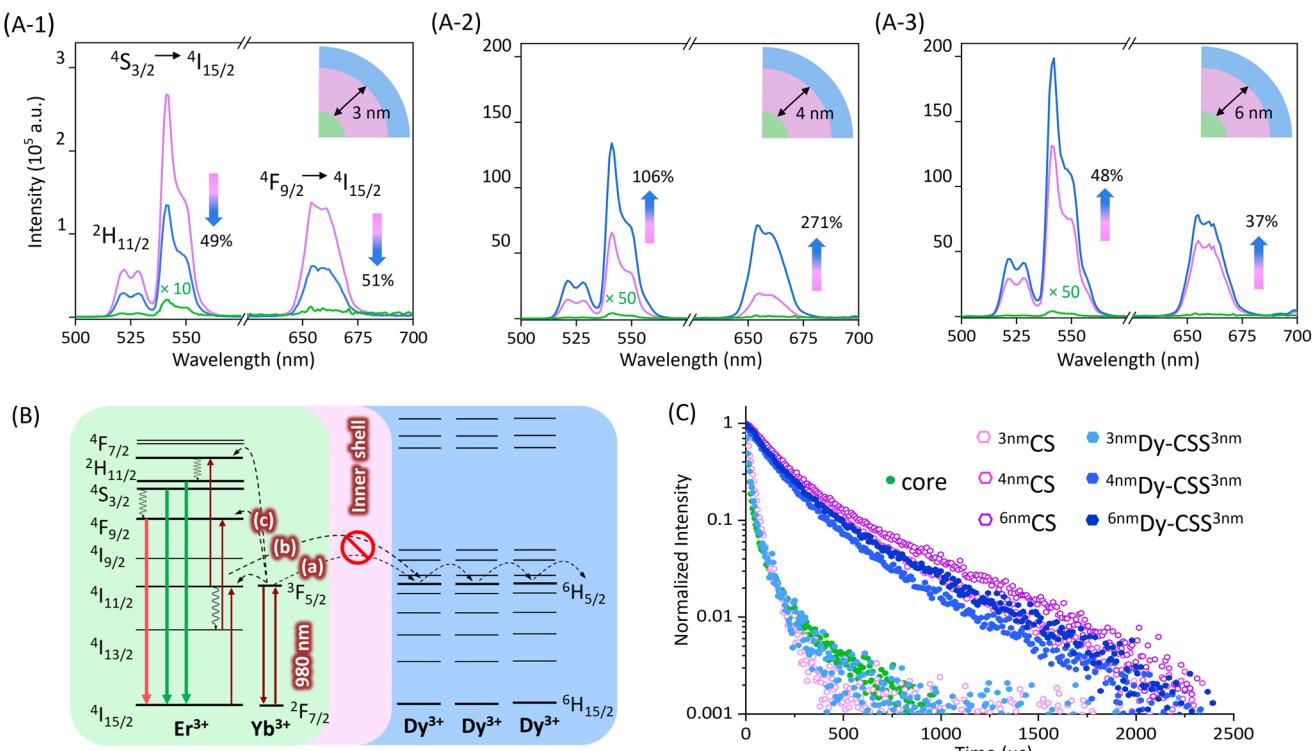
Fig. 2 (A) UC spectra of OA-capped ^{3nm}Dy-CSS^{3nm} (1), ^{4nm}Dy-CSS^{3nm} (2), and ^{6nm}Dy-CSS^{3nm} (3) NPs (blue) as well as their corresponding core (green) and CS (pink) NPs. All spectra were obtained under 980 nm laser excitation. Power density = 6.0 W cm^{-2}, [NP] = 5 mg mL^{-1} in toluene. (B) Partial energy level diagram for Er^{3+}/Yb^{3+} and Dy^{3+}, schematically showing how the addition of an inner shell physically separates Er^{3+}/Yb^{3+} from Dy^{3+} ions, thus, preventing Dy^{3+}-induced loss of the UC. Solid lines are radiative transitions, dotted lines indicate energy transfer, and wavy lines are non-radiative transitions. (C) Luminescence decay curves of the Yb^{3+} emission under 980 nm excitation obtained from core, CS, and CSS NPs.

spectroscopy.[9] As schematically shown in Fig. 2B, in close vicinity to Dy^{3+} ions, the $^2F_{5/2}$ excited state of Yb^{3+} and the $^2I_{11/2}$ excited state of Er^{3+} can be depopulated *via* resonant energy transfer to the excited $^6H_{5/2}$ level of Dy^{3+} (steps (a) and (b)). This depopulation of the excited Yb^{3+} and intermediate Er^{3+} levels compromise efficient UC to the emitting Er^{3+} levels (step (c)), ultimately resulting in loss of UC emission. The added inner shell acts as a barrier hampering the Yb^{3+} (and Er^{3+}) $\rightarrow$ Dy^{3+} energy transfer, restoring Er^{3+} UC. In order to confirm the UC loss mechanism, two reference samples were synthesized, namely, cubic (α)-phase NaDyF$_4$:Yb,Er core NPs and β-phase NaGdF$_4$:Yb,Er/NaDyF$_4$ NPs (Dy-CS) (Fig. S4†). As shown in Fig. S5,† not surprisingly, the emission of Er^{3+} was completely lost when the emitting Ln^{3+} ions were co-doped into the NaDyF$_4$ host. UC loss still took place upon separation of Er^{3+}/Yb^{3+} and Dy^{3+} into the β-NaGdF$_4$:Yb,Er core and a NaDyF$_4$ shell (Dy-CS).

Confirmation of the proposed quenching mechanism was obtained by determining the excited state lifetime of Yb^{3+} in the series of core, CS and CSS NPs under investigation. Therefore, the time-dependent emission of Yb^{3+} under 980 nm excitation was monitored at the shoulder of the ion's emission at 940 nm.[42,43]

The decay curves and respective lifetime values are given in Fig. 2C and Table 1. The small core NPs exhibited a relatively

Table 1 Lifetime values extracted from the decay curves of the Yb^{3+} emission under 980 nm

Sample	Inner shell thickness (nm)	Lifetime (μs)
Core	NA	25.5
^{3nm}CS	*ca.* 3	33.3
^{3nm}Dy-CSS^{3nm}		26.1
^{4nm}CS	*ca.* 4	207.6
^{4nm}Dy-CSS^{3nm}		175.8
^{6nm}CS	*ca.* 6	251.3
^{6nm}Dy-CSS^{3nm}		207.6

short lifetime of 25.5 μs due to surface quenching, which was slightly prolonged to 33.3 μs when an undoped shell of 3 nm was added (^{3nm}CS). Yet, growth of an additional NaDyF$_4$ shell shortened the lifetime to 26.1 μs (^{3nm}Dy-CSS^{3nm}). This decrease in lifetime is in line with the reduced Er^{3+} emission (Fig. 2(A-1)). As expected, the addition of a thicker undoped NaGdF$_4$ shell led to a significantly longer lifetime (^{4nm}CS: 207.6 μs). The observed increase in UC emission intensity upon growth of an additional outer NaDyF$_4$ shell (^{4nm}Dy-CSS^{3nm}) suggests efficient shielding of the Yb^{3+}/Er^{3+} ion pair from Dy^{3+} (Fig. 2(A-2)) as well as additional protection against surface loss processes. Hence, a prolonged Yb^{3+} lifetime might be expected. Conversely, the decay time decreased to 175.8 μs

for ^{4nm}Dy-CSS^{3nm} NPs, indicating continuous depopulation of the $^2F_{5/2}$ Yb^{3+} level by Dy^{3+} ions. To assess whether an even thicker undoped shell could fully overcome energy transfer to Dy^{3+}, the optical properties of ^{6nm}Dy-CSS^{3nm} NPs with a *ca.* 6 nm thick inner shell were analyzed. As expected, emission spectra did not indicate any UC poisoning effect of Dy^{3+}, and the sample exhibited the strongest emission intensity among all the investigated NPs due to its overall thick shell (NaGdF$_4$ + NaDyF$_4$: 8.2 nm) (Fig. 2(A-3)). Still, time-dependent measurements revealed that energy transfer to Dy^{3+} was not fully suppressed, as indicated by the shortening of the Yb^{3+} lifetime upon shelling with NaDyF$_4$ (251.3 μs for ^{6nm}CS *versus* 207.6 μs for ^{6nm}Dy-CSS^{3nm}). The influence of the NaDyF$_4$ shell on the UC emission was further demonstrated by power-dependent photoluminescence spectroscopy. Power plots and a brief discussion are provided in the ESI (Fig. S6†). Overall, based on the Er^{3+} emission spectra and Yb^{3+} lifetimes of ^{4nm}Dy-CSS^{3nm} and ^{6nm}Dy-CSS^{3nm}, a 4 nm inner shell thickness was deemed sufficiently efficient to suppress the most severe Dy^{3+}-induced UC loss, resulting in bright UC emitters, despite some remaining energy transfer from Yb^{3+} to Dy^{3+}. Herein, the increased shell thickness is suggested to play a dual role. First, the Yb^{3+} → Dy^{3+} energy transfer is hindered by the barrier layer, resulting in more efficient UC to the Er^{3+} emitting levels. Second, the overall shell (NaGdF$_4$ + NaDyF$_4$) around the emitting core reaches a thickness that was previously reported as highly efficient in reducing non-radiative depopulation of the emitting Er^{3+} levels, which is supported by increasing lifetimes of the green ($^4S_{3/2}$) and red ($^4F_{9/2}$) emitting excited states (Fig. S7 and S8†).[44] Ultimately, both aspects together result in not only restored but enhanced UC emission, demonstrated here – to the best of our knowledge – for the first time.

To explore the effect of the NaDyF$_4$ shell on the probes' performance, particularly MRI T_2 and CT capabilities (*vide infra*), additional Dy-CSS NPs were synthesized. Given the good optical performance of ^{4nm}Dy-CSS^{3nm}, exhibiting a *ca.* 4 nm thick inner shell, two samples with an outer NaDyF$_4$ shell of varying thickness on ^{4nm}CS NPs were synthesized. This resulted in a total set of three samples of comparable core size and inner shell thickness, yet, varying outer shells of *ca.* 1 nm (^{4nm}Dy-CSS^{1nm}), 3 nm (^{4nm}Dy-CSS^{3nm}), and 4 nm (^{4nm}Dy-CSS^{4nm}), respectively (Table S1†). The morphology, size, crystalline phase, and UC spectra of these samples are shown in Fig. S9–S11.†

Rendering the NPs water-dispersible: citrate-capping

To explore MRI and CT capabilities, the OA-capped NPs were transferred to the aqueous milieu by ligand exchange with trisodium citrate molecules.[21,45] The successful citrate capping was confirmed by Fourier transform infrared (FTIR) spectroscopy, and the morphology and the crystalline phase remained (Fig. S12†). The cytotoxicity of Cit-^{4nm}Dy-CSS^{3nm} NPs against human lung adenocarcinoma cells (A549) was assessed using the flow cytometry assay. As shown in Fig. S13,† the cell viability remained 95% for all NP concentrations, indicating low cytotoxicity of citrate-capped NPs at concentrations below

500 μg mL^{-1}. Despite some expected loss of photoluminescence intensity upon dispersion of the NPs in water compared to their OA-capped counterparts in toluene, Cit-^{4nm}Dy-CSS^{3nm} NPs still showed bright UC emission and NIR emission at 1570 nm, which stems from the $^4I_{13/2} \rightarrow {}^4I_{15/2}$ Er^{3+} transition (Fig. S14†). Moreover, the NPs exhibited good luminescence stability after incubation in water and phosphate-buffered saline (PBS) for 24 h at 37 °C (Fig. S15†). Er^{3+}-doped UC emitters are well-known for their suitability to act as ratiometric nanothermometers, using the luminescence intensity ratio (LIR) between the two green emission bands as the thermal parameter.[46] While nanothermometry was not the major focus of this study, we stepped forward to briefly explore this avenue, assessing the potential of the prepared NPs for thermal sensing and imaging. Temperature-dependent measurements from 15 to 50 °C unveiled decent thermal sensing behavior in the physiologically relevant temperature range, with a relative thermal sensitivity S_r of 1.1% °C^{-1} at 40 °C. Data and a short discussion are provided in the ESI (Fig. S16†).

Citrate-capped Dy-CSS NPs for MR imaging

The Dy^{3+} ion has the potential to be a T_2-weighted MRI contrast agent due to its high magnetic moment. To study the effect of the NaDyF$_4$ shell thickness of the obtained Cit-Dy-CSS NPs on T_2 contrast performance, T_2 and T_1 relaxivities (r_2 and r_1) were measured at 7 T. As shown in Fig. 3A, the T_2-weighted MRI signals obtained from Cit-Dy-CSS NPs changed from brighter to darker when the concentration of Dy^{3+} increased, indicating the potential of these NPs to act as T_2 contrast agents. The relaxivity values were extracted from the slopes of the linear fits of the relaxation rates R_2 and R_1 (=1/T_2 and 1/T_1) against the molar concentration of Dy^{3+} ions of the NP dispersions as obtained from inductively coupled plasma optical emission spectroscopy (ICP-OES) (Fig. 3B – r_2; Fig. S17† – r_1; all values are summarized in Table 2). Similar r_2 values were obtained for Cit-^{4nm}Dy-CSS^{1nm} (260.0 mM^{-1} s^{-1}) and Cit-^{4nm}Dy-CSS^{3nm} NPs (256.9 mM^{-1} s^{-1}), while a significant increase of r_2 to 442.1 mM^{-1} s^{-1} was observed when the NaDyF$_4$ shell thickness increased to 4 nm (Cit-^{4nm}Dy-CSS^{4nm}). This increase in r_2 was ascribed to the increasing amount of Dy^{3+} ions in the sample upon growth of a thicker outer shell, resulting in a higher Dy^{3+}-to-Gd^{3+} ratio (Fig. S18†). Larger particle sizes have previously been reported to result in more pronounced T_2 contrast enhancement, as demonstrated for different-sized NaDyF$_4$ NPs.[27,28] Even though the direct comparison with data from the literature is difficult given the different NP architectures under investigation (CSS in this study *versus* previously investigated core-only NPs), the larger size of the Cit-^{4nm}Dy-CSS^{4nm} NPs might also contribute to the observed T_2 contrast enhancement. On the contrary, the r_1 values decreased with increasing NaDyF$_4$ shell thickness (Fig. S17† and Table 2). It is important to recall that NdGdF$_4$ was used as host matrix for the core and inner shell of the CSS-NPs. Gd^{3+} ions are well known for their T_1 MRI capabilities when in close vicinity to water protons. Thus, the Gd^{3+}
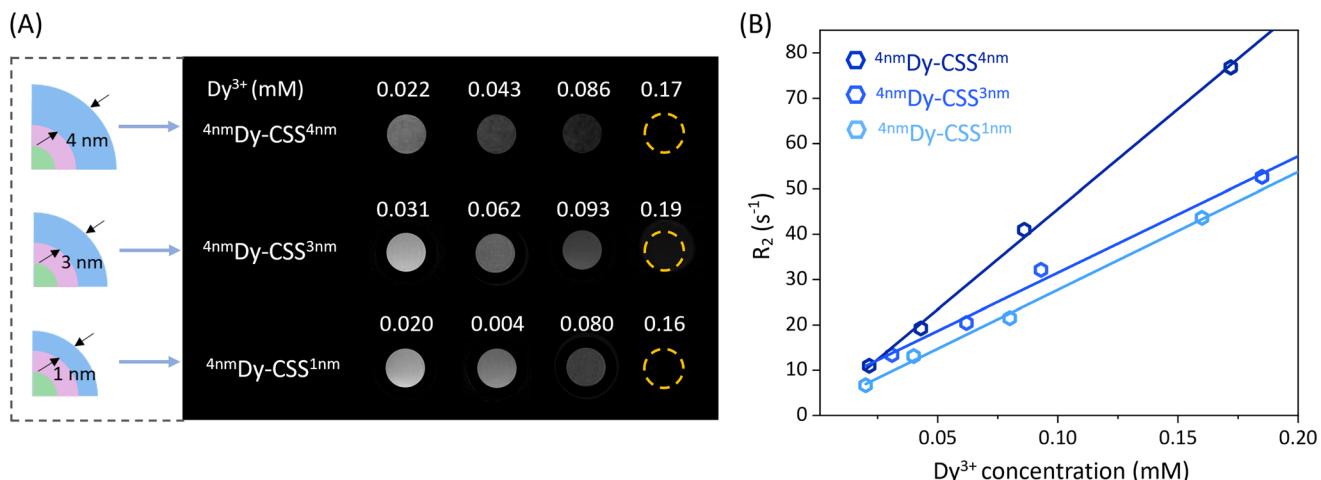
Fig. 3 (A) T_2-Weighted MR images of Cit-Dy-CSS NPs with varying NaDyF$_4$ outer shell thickness (Cit-^{4nm}Dy-CSS^{1nm}, Cit-^{4nm}Dy-CSS^{3nm} and Cit-^{4nm}Dy-CSS^{4nm}) as a function of the Dy^{3+} concentration. (B) Relaxation rate R_2 (=$1/T_2$) of water protons plotted against the molar concentration of Dy^{3+} at 7 T. Solid lines are linear fits.

Table 2 Relaxivity values r_2 and r_1 of Cit-Dy-CSS NPs at 7 T. Relaxivity values and the associated errors were obtained from the linear fitting procedure of the data sets reported in Fig. 3 and S17, S19†

Sample	Size (nm)	r_2 (mM^{-1} s^{-1})	r_1 (mM^{-1} s^{-1})	r_2/r_1
^{4nm}Dy-CSS^{1nm}	16.9	260.0 ± 9.8	6.5 ± 0.1	40.0
^{4nm}Dy-CSS^{3nm}	18.1	256.9 ± 17.7	4.6 ± 0.1	55.8
^{4nm}Dy-CSS^{4nm}	21.9	442.1 ± 22.1	3.3 ± 0.2	134.0
^{6nm}Dy-CSS^{3nm}	22.0	116.0 ± 10.0	2.5 ± 1.1	46.4

ions in the core and inner shell might influence the overall MRI performance of the CSS-NPs. Indeed, the highest r_1 value was obtained for Cit-^{4nm}Dy-CSS^{1nm} NPs with a very thin outer shell. Such thin shelling might be less efficient and prone to cation intermixing, resulting in Gd^{3+} ions close to the NP surface where they can interact with water protons, contributing to higher r_1 value. Thicker NaDyF$_4$ shells provided greater shielding of the Gd^{3+} ions in the inner shell, resulting in lower r_1 values. Overall, the resultant r_2/r_1 ratios increased from 40.0 to 55.8 and 134.0 with increasing NaDyF$_4$ shell thickness. As larger r_2/r_1 ratios provide for higher signal-to-noise and more robust contrast enhancement in T_2-weighted images,[27] Cit-^{4nm}Dy-CSS^{4nm} NPs with the thickest outer shell are the most promising among the studied T_2 MRI CA candidates.

The effect of the inner NaGdF$_4$ shell thickness on the T_2 contrast behavior was also investigated. As shown in Fig. S19,† Cit-^{4nm}Dy-CSS^{3nm} NPs exhibited a higher r_2 value (256.9 mM^{-1} s^{-1}) than Cit-^{6nm}Dy-CSS^{3nm} NPs (116.0 mM^{-1} s^{-1}), which can be ascribed to the relatively higher Dy^{3+} content in the sample (Fig. S18†). In line, a larger r_2/r_1 ratio was obtained for Cit-^{4nm}Dy-CSS^{3nm} (55.8) than for Cit-^{6nm}Dy-CSS^{3nm} (46.4) NPs, demonstrating the importance to not only tune the outer NaDyF$_4$ but also inner NaGdF$_4$ shell.

Noteworthy, all the r_2 values of Cit-Dy-CSS NPs are higher than those of commercial iron oxide-based T_2 contrast agents

(Combidex: 60.0 mM^{-1} s^{-1}, Feridex: 93.0 mM^{-1} s^{-1}) and other comparable sized Dy-based NPs (Table S2†).[5,10,26,27,35,47–54] These observations are promising with respect to the potential use of Dy-CSS NPs T_2 CAs. Particularly, high relaxivity CAs are generally considered beneficial as they can allow for the administration of lower doses, ultimately contributing to lower toxicity risks.[55]

Citrate-capped Dy-CSS NPs for CT imaging

Owing to the relatively high K-edge values and X-ray attenuation coefficients of the Ln ions, Cit-Dy-CSS NPs hold potential for CT imaging. To assess their CT contrast performance, we first used X-ray spectrometry (Fig. S20†) to compare the X-ray absorption efficacy of Cit-Dy-CSS NPs to that of iohexol (a widely used clinical CT CA). With the iodine K-edge at 33.3 keV, iohexol absorbs X-ray photons most effectively in the range 35–50 keV.[56] In comparison, Cit-Dy-CSS NPs absorb more photons in a higher energy region (50–120 keV) due to the higher K-edge values of Gd (50.2 keV) and Dy (53.8 keV). In an alternative approach to demonstrate the X-ray absorption behavior of iohexol and Cit-Dy-CSS NPs (Cit-^{4nm}Dy-CSS^{3nm}, Cit-^{6nm}Dy-CSS^{3nm}), radiography imaging was performed across a range of X-ray source voltages from 70 to 120 kV. These voltages are consistent with conditions used in clinical applications. As shown in Fig. S21A,† CT values (Hounsfield units, HU) for iohexol were highest at a source voltage of 70 kV, followed by a continuous decrease with voltage increase to 120 kV. This is expected given the optimized performance of iohexol at lower energies.[57] On the contrary, the CT values of Cit-Dy-CSS NPs displayed an initial increase in CT values when the voltage increased from 70 to 110 kV, followed by a decrease at 120 kV (Fig. S21B/C†). This decrease in CT values at higher voltage was caused by the mismatch of the K-edge values of Gd and Dy in the high-energy region. The highest CT value obtained for Cit-^{6nm}Dy-CSS^{3nm} NPs at 110 kV was 1080 HU

(A)

(B)
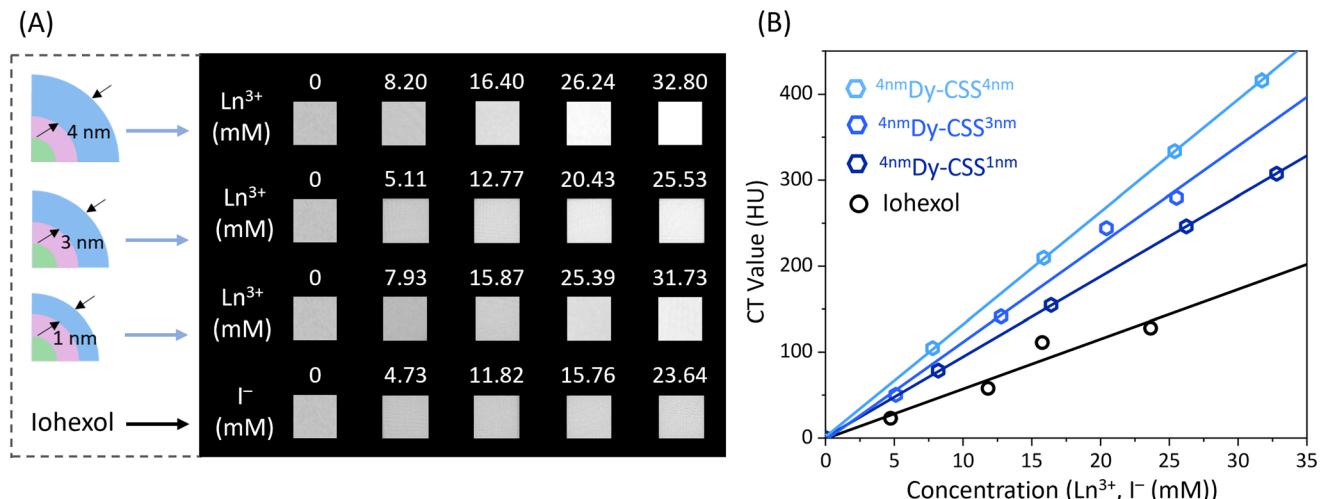
Fig. 4 (A) CT images of Cit-Dy-CSS (Cit-^{4nm}Dy-CSS^{1nm}, Cit-^{4nm}Dy-CSS^{3nm}, and Cit-^{4nm}Dy-CSS^{4nm}) NPs and clinically used CT CA iohexol at different concentrations. (B) CT values for different concentrations of Cit-Dy-CSS NPs dispersed in water and iohexol solutions. Solid lines are linear fits.

(Ln^{3+} ion concentration, *i.e.*, sum of Gd^{3+}, Dy^{3+}, Yb^{3+} and Er^{3+} = 94.2 mM) compared to 850 HU of iohexol (I^- ion concentration = 157.6 mM). Normalization of the CT values to the concentration of the corresponding contrast agent, revealed more than two-times higher values for the Cit-Dy-CSS NPs than for iohexol between 100 and 120 kV (Fig. S21D†). These findings demonstrate the potential of Cit-Dy-CSS NPs as CT CA candidates with higher contrast efficacy compared to iohexol at 110 kV and the advantage that X-rays optimized for the K-edge of the Ln^{3+} have lower potential for tissue damage than those optimized for the K-edge of iodine.[36]

Encouraged by the results of radiography imaging, CT phantom imaging measurements of Cit-Dy-CSS NPs and iohexol were performed at 110 kV. Herein, samples with thinner and thicker NaDyF$_4$ shells were investigated to assess any potential effect that the outer shell thickness might have on CT performance. As shown in Fig. 4A, with similar CA concentrations, all Cit-Dy-CSS NPs produced brighter CT signals than iohexol. The obtained CT values increased linearly with the concentration for Cit-Dy-CSS NPs and iohexol (Fig. 4B), and the slopes extracted from the linear fits are shown in Table 3. Among the three Cit-Dy-CSS samples, the slope values increased with the NaDyF$_4$ shell thickness increasing from 1 nm to 4 nm (9.4 ± 1.3 HU mM^{-1} for Cit-^{4nm}Dy-CSS^{1nm}, 11.4 ± 0.5 HU mM^{-1} for Cit-^{4nm}Dy-CSS^{3nm} and 13.1 ± 0.05 HU mM^{-1} for Cit-^{4nm}Dy-CSS^{4nm}). These findings can be ascribed to the

relatively larger amount of Dy^{3+} with increasing NaDyF$_4$ shell thickness, resulting in a higher Dy^{3+}-to-Gd^{3+} ratio (Fig. S18†), ultimately allowing for higher X-ray attenuation. Noteworthy, all the slope values obtained from Cit-Dy-CSS NPs were higher than that of iohexol (5.8 ± 1.3 HU mM^{-1}), indicating that Cit-Dy-CSS NPs exhibit higher contrast efficacy than iohexol.

Conclusions

With the goal to design a NP candidate to act as multimodal probe that merges upconversion and T_2 MRI capabilities, a set of Dy-CSS NPs doped with Er and Yb was synthesized using a microwave-assisted approach. Careful tuning of the microwave reaction conditions allowed for controlled inner shell thicknesses from *ca.* 3 to 6 nm. Such control is crucial to physically separate the luminescent Er^{3+}/Yb^{3+} ion pair in the core from the magnetic Dy^{3+} ions in the outer shell, ultimately preventing UC loss. The mechanism of UC loss was investigated in detail by evaluating the Er^{3+} upconversion intensities and the excited state lifetimes of Yb^{3+} and Er^{3+} as a function of the inner shell thickness. Based on the Er^{3+} emission spectra and Yb^{3+} lifetimes, an isolating 4 nm inner shell between the emitting core and the NaDyF$_4$ outer shell suppressed energy transfer from Yb^{3+} to Dy^{3+}, followed by Dy^{3+}-mediated energy migration and loss at the NP surface. As a result, UC excitation of the Er^{3+} ions was restored, and enhanced UC emission was observed upon addition of the outer NaDyF$_4$ shell. Noteworthy, the microwave-assisted strategy led to CSS architectures, while keeping the overall NP size close to 20 nm. In addition, the effect of the outer NaDyF$_4$ shell thickness on the particles' magnetic and CT performance was investigated. MRI T_2 relaxivity measurements performed *in vitro* at 7 T on Cit-Dy-CSS NPs revealed that the Cit-^{4nm}Dy-CSS^{4nm} NPs with the thickest outer shell (4 nm) exhibited the highest r_2 value and r_2/r_1 ratio, indicating a superior T_2 contrast effect compared to commer-

Table 3 CT capabilities of Cit-Dy-CSS NPs and iohexol solution measured at 110 kV

Sample	Size (nm)	Slope of the linear fit (HU mM^{-1})
^{4nm}Dy-CSS^{1nm}	16.9	9.4 ± 0.03
^{4nm}Dy-CSS^{3nm}	18.1	11.4 ± 0.5
^{4nm}Dy-CSS^{4nm}	21.9	13.1 ± 0.05
Iohexol	—	5.8 ± 1.3

cial iron oxide-based CAs and other Dy-based T_2 CAs. In addition, the CT values of Cit-Dy-CSS NPs increased with increasing outer $NaDyF_4$ shell thickness. Interestingly, all investigated Cit-Dy-CSS NPs exhibited advanced CT contrast efficacy compared to commercially used iohexol at an X-ray energy of 110 keV. Our results demonstrate the promise of the designed Dy-CSS NPs to act as potential multimodal imaging probe. The concept of fabricating multilayer NPs by use of microwave-assisted routes that offer control over shell thicknesses also provides insights for the future architecture design of Ln-based materials for their *e.g.*, biomedical applications and beyond.

Experimental

Chemicals

Gadolinium oxide (Gd_2O_3, 99.999%), ytterbium oxide (Yb_2O_3, 99.998%) and erbium oxide (Er_2O_3, 99.99%) were purchased from Alfa Aesar. Dysprosium oxide (Dy_2O_3, 99.9%) was purchased from Sigma Aldrich. Trifluoroacetic acid (CF_3COOH, H-TFA, 98%), sodium trifluoroacetate (CF_3COONa, Na-TFA, 98%), oleic acid ($CH_3(CH_2)_7CH{=}CH(CH_2)_7COOH$, OA, 90%), oleylamine ($CH_3(CH_2)_7CH{=}CH(CH_2)_7CH_2NH_2$, OAm, 70%), 1-octadecene ($CH_3(CH_2)_{15}CH{=}CH_2$, ODE, 90%) and sodium citrate dihydrate (99%), 1,3-diphenylisobenzofuran ($C_{20}H_{14}O$, 97%) were purchased from Sigma Aldrich. Iohexol ($C_{19}H_{26}I_3N_3O_9$, 300 mg I per mL) was purchased from GE Healthcare. Ethanol (99%) was purchased from Commercial Alcohols. Acetone and hexane (analytical grade) were purchased from Fischer Chemicals. Toluene (99.8%) and hydrochloric acid (HCl, 36.5%) were purchased from Fisher Scientific. All chemicals were used as received.

Microwave-assisted synthesis of core β-NaGdF₄:Yb,Er NPs

The synthesis of the NPs was performed using a modified version of the microwave-assisted thermal decomposition of lanthanide trifluoroacetate, $[Ln(TFA)_3]$, precursors (Ln = Gd^{3+}, Yb^{3+}, Er^{3+} and Dy^{3+}) previously reported by our group.[39] Briefly, for the synthesis of β-$NaGdF_4$ NPs doped with 20 mol% Yb^{3+} and 2 mol% Er^{3+}, 0.625 mmol of $[Ln(TFA)_3]$ were prepared mixing Gd_2O_3 (0.244 mmol), Yb_2O_3 (0.0625 mmol), and Er_2O_3 (0.00625 mmol) in a 50 mL three-neck round-bottom flask. A 10 mL amount of a 1 : 1 TFA-to-H_2O mixture was added, the slurry was refluxed at 95 °C until it became clear and dried at 60 °C overnight. Subsequently, 1.875 mmol of Na-TFA (3 : 1 Na^+-to-Ln^{3+} ion ratio) was added to the synthesized $[Ln(TFA)_3]$ along with 2.5 mL of oleic acid, 2.5 mL of oleylamine and 5 mL of 1-octadecene. This mixture was degassed at 120 °C under vacuum for 30 min. Subsequently, the degassed precursor solution was transferred to a 35 mL microwave vessel, purged with N_2 and tightly sealed. The vessel was inserted into a CEM Discovery SP microwave reactor. The precursor solution was heated to 270 °C for 1 s, followed by rapid cooling to 250 °C, the temperature at which the reaction was held for 10 min, and subsequent cooling to 50 °C. Following the syn-

thesis, the reaction mixture was washed with a 1 : 3 hexane-to-ethanol mixture and centrifuged at RCF = 6595*g* for 20 min. The product was then washed with a 1 : 3 toluene-to-acetone mixture and centrifuged using the same conditions. After purification, the NPs were dispersed and stored in 5 mL of toluene for further use. NaF as a potential by-product can be removed by redispersing the NPs in 5 mL of ethanol prior to the addition of 5 mL of water, followed by precipitation *via* centrifugation. Obtained NPs were washed one more time with 10 mL of ethanol before being stored in 5 mL of toluene for further characterization. In case of loss of dispersion stability of the NPs following this washing procedure, dispersibility in toluene can be restored by adding 0.2 mL of OA to the NP dispersion and subsequent stirring at room temperature overnight.

Microwave-assisted synthesis of β-NaGdF₄:Yb,Er/NaGdF₄ core/shell NPs

An undoped $NaGdF_4$ shell was grown onto the doped core NPs by subjecting the NPs to a second microwave-assisted treatment, adding $[Gd(TFA)_3]$ as shell precursor. 0.625 mmol of the shell precursor was prepared as described above, using Gd^{3+} as sole lanthanide. Subsequently, 1.875 mmol of Na-TFA (3 : 1 Na^+-to-Gd^{3+} ratio), 4 mL of ODE and 5 mL of OA were added to the shell precursor. The reaction mixture was degassed under vacuum at 120 °C for 30 min. The shell thickness was controlled by adjusting the ratio between the core NPs acting as seeds for shell growth and the shell precursor. More specifically, 100 mg, 40 mg, or 30 mg of the core NPs, prepared in the previous step, were used as seeds to grow shells of *ca.* 3, 4, and 6 nm, respectively. Therefore, the respective amount of core NPs was firstly dispersed in 1 mL of ODE (note: in contrast to the core synthesis, no OAm was used to grow the $NaGdF_4$). Subsequently, this 1 mL of ODE containing core NPs and 9 mL of the degassed shell precursor solution were transferred to a 35 mL microwave vessel, purged with N_2, and tightly sealed. The vessel was inserted into a CEM Discover SP microwave reactor, and the mixture was heated to 250 °C and held for 10 min under stirring. The cooling and washing procedure as well as storage of the obtained core/shell NPs were as described above for the core NPs.

Microwave-assisted synthesis of β-NaGdF₄:Yb,Er/NaGdF₄/NaDyF₄ core/shell/shell NPs

The procedure to grow the outer shell of $NaDyF_4$ was similar to that used for the synthesis of the core/shell NPs, except that $[Dy(TFA)_3]$ was used as precursor. The shell precursor, 0.625 mmol of $[Dy(TFA)_3]$, was prepared as described above, using Dy^{3+} as sole lanthanide. Then, 1.25 mmol of Na-TFA (2 : 1 Na^+-to-Dy^{3+} ratio), 4 mL of ODE and 5 mL of OA were added to the precursor. The reaction mixture was degassed under vacuum at 120 °C for 30 min. The shell thickness was controlled by adjusting the ratio between the core/shell NPs acting as seeds for shell growth and the shell precursor. More specifically, 160 mg, 120 mg, or 90 mg of the core/shell NPs, prepared in the previous step, were used as seeds to grow

shells of *ca.* 1, 3, and 4 nm, respectively. Subsequently, the 1 mL of ODE containing core/shell NPs and 9 mL of the degasses shell precursor solution were transferred to a 35 mL microwave vessel, purged with N_2, and tightly sealed. The vessel was inserted into a CEM Discover SP microwave reactor, the mixture was heated to 250 °C and held for 10 min under stirring. The cooling and washing procedure as well as storage of the obtained core/shell/shell NPs were as described above for the core NPs.

Surface modification with citrate groups

Trisodium citrate was used to replace oleate (OA) groups at the surface of the as-prepared $NaGdF_4$:Yb,Er/$NaGdF_4$/$NaDyF_4$ NPs following a modified version of previously reported protocols.[21] Briefly, 70 mg of NPs was dispersed in 5 mL of hexane. Then, 5 mL of 0.2 M trisodium citrate buffer (pH = 2.7) was added to the NP colloidal dispersion. The two-phase mixture was stirred for 4 h at 45 °C. Subsequently, the aqueous/organic mixture was poured into a separatory funnel, and the aqueous phase now containing the NPs was isolated. The NPs were precipitated with acetone (aqueous to organic phase ratio: 1 : 3) and centrifuged at 6595g for 20 min. The organic solvent was removed, and the recovered NPs were re-dispersed in 5 mL of trisodium citrate buffer (pH = 7). The dispersion was stirred for 1 h, followed by three washing steps using water and acetone for precipitation and subsequent centrifugation under aforementioned conditions. The obtained citrate-capped NPs were stored in 5 mL of water.

Characterization techniques

To determine the crystalline phase of the NPs, powder X-ray diffraction (XRD) analysis was performed using a Rigaku Ultima IV Diffractometer or a Bruker D8 Endeavor (Cu Kα, λ = 1.5401 Å), operating at 44 kV and 40 mA (step size: 0.02°, scan speed: 1° min^{-1}). Therefore, the NPs were deposited on a glass slide from their suspension. The morphology and size distribution of the obtained NPs were investigated by transmission electron microscopy (TEM, FEI Tecnai Spirit). The samples were dispersed on a Formvar/carbon film supported on a 300-mesh copper TEM grid. Size distributions (mean size ± standard deviation) of the samples were derived from TEM images using the software ImageJ. The respective size distributions were obtained analysing 200 particles per sample. The presence of the citrate ligands at the particles' surface was investigated by Fourier-transform infrared (FTIR) spectroscopy, using a Cary 630 FTIR spectrometer in ATR mode (Diamond ATR crystal), with acquisition of 128 scans and resolution of 4 cm^{-1}. Dynamic light scattering (DLS) and zeta (ζ-) potential measurements were carried out on NPs dispersed in water using a Malvern Zetasizer Nano-ZS.

Investigation of the steady-state photoluminescence properties of the NPs in suspension (5 mg mL^{-1} in toluene or water) was carried out in a quartz cuvette (suitable spectral range from 200 to 2500 nm, 1 cm optical path) inserted into the Peltier temperature sample holder of a QuantaMaster 8075-21 spectrofluorometer from HORIBA, equipped with double grating emission monochromators, a red-extended photomultiplier detector R13456 PMT (185 to 980 nm) and a liquid nitrogen cooled InAs detector (1000 to 3450 nm). The NIR continuous excitation was performed using a 980 nm continuous-wave laser diode (power densities used to trigger upconversion and NIR emission were 6.0 W cm^{-2} and 33.3 W cm^{-2}, respectively). Power-dependent studies were performed using the same setup described above, including different neutral density filters to stepwise reduce the incident laser power. For temperature-dependent studies, the temperature of the sample was changed from 15 °C to 50 °C in 5° steps, using the Peltier temperature sample holder with a liquid cooling system. At each step, the temperature was allowed to stabilize for 15 min prior to the measurements. Photoluminescence lifetimes were obtained by time-resolved spectroscopy, using the 980 nm laser diode in pulsed mode. Lifetime values were obtained by integration of the area under the normalized decay curves. For all the optical measurements, filters were placed in front of detectors. A short-pass 775 nm filter was used for visible emission acquisition, while a long-pass 1025 nm filter was used for NIR emission detection.

The Ln^{3+} ion concentration in the samples was determined with an Agilent ICP-OES spectrometer. Therefore, 10 mg of Dy-CSS NPs was added to a mixture of 0.5 mL of concentrated HNO_3 and 1.5 mL of concentrated HCl, followed by heating at 80 °C for 5 h ensuring that all NPs were digested. Flow conditions of the Agilent ICP-OES spectrometer were as follows: nebulizer flow = 0.7 L min^{-1}, plasma flow = 12 L min^{-1}, auxiliary flow = 1 L min^{-1}.

MRI relaxivity measurements were performed on a 7.0 T preclinical MRI instrument (Discovery MR901, Agilent/General Electric). T_1 measurements were measured using a classical inversion recovery method with the following parameters: repetition time TR = 15 000 ms, echo time TE = 6.4 ms, eight inversion recovery times (TI = 50, 100, 400, 800, 1200, 2000, 3000 and 4000 ms), field of view (FOV) = 8 × 8 mm^2, slice thickness = 3 mm, matrix = 128 × 128. T_2 measurements were performed using a Carr–Purcell–Meiboom–Gill (CPMG) sequence with the following parameters: TR = 5000 ms, FOV = 10 × 10 mm^2, slice thickness = 3 mm, matrix = 128 × 256, TE = 13, 26.1, 39.1, 52.2, 65.2, 78.2, 91.3 and 104 ms. T_2-Weighted images were obtained on the same MR instrument using the following parameters: TR = 5000 ms, FOV = 10 × 10 mm^2, slice thickness = 3 mm, matrix = 128 × 256, TE = 52 ms. T_1 and T_2 relaxation times (R_1 and R_2) were calculated using single exponential fitting of the data extracted from mapping images for different concentrations of Cit-Dy-CSS NPs in water.

X-ray absorption spectroscopy measurements were conducted using a Hamamatsu L12161-07 tungsten source collimated to a 1 mm beam. A 0.6 mm Cu filter was used to harden the beam. The source current was 150 μA and the source voltage was 150 kV. An Amptek Cd–Te 25 mm^2 spectrometer was used in combination with Amptek PX-5 Digital Pulse Processor. Each spectrum has an acquisition time of 120 s. Radiograph imaging measurements were performed with a PXS MicroCT system (Pinnacle X-ray Solutions Inc.) consisting

of a Hamamatsu L12161-07 source coupled with a Varian PaxScan 1313DX digital image detector. Conditions of the source were 150 μA current with different voltages, *i.e.*, 70, 80, 90, 100, 110 and 120 kV. The X-ray beam was hardened using a 3.3 mm Al filter. Each image consists of the average of 20 frames taken at 2 frame per second for a total acquisition time per image of 10 seconds. ImageJ 1.52c was used to determine an average attenuation value from an area within the frame. Images of water and an empty (air) vial were obtained as reference to calculate the Hounsfield unit (HU) values following eqn (1):[58]

$$ HU = \frac{(\mu_{material} - \mu_{water})}{\mu_{water}} \times 1000 \qquad (1) $$

where μ is the linear X-ray attenuation coefficient of each material, obtained from the following equation:[58]

$$ I = I_0 \times e^{-\mu x} \qquad (2) $$

where I is the X-ray output intensity from the investigated material (*i.e.*, iohexol or Dy-CSS NPs), I_0 is the X-ray input intensity (*i.e.*, the intensity obtained from an empty (air) vial), and x is the thickness of the material (*i.e.* the diameter of the vial, 1 cm). The CT images were collected using a Hamamatsu L12161-97 source coupled with a Varian PaxScan 1313DX flat panel detector. Conditions of the source were 110 kV voltage and 250 μA current. The X-ray beam was hardened using a 3.3 mm Al filter. Data acquisition was done using PXS iRAD software (v7.0.0.12) with each image consisting of the average of 10 frames, each frame being captured at 15 fps (or 0.067 s exposure per frame). Prior to the acquisition, flat field correction of the panel was obtained as well as a bright (X-ray on, no target) and a dark file (X-ray off) for reconstruction calibration. A total of 360 images were taken with a 1° clockwise stepping. The obtained images were imported using VGS-studio-max software for the reconstruction. Average values of a volume within water-filled and the empty vials were obtained with ImageJ 1.52c and used to determine the Hounsfield unit (HU) values.

Cytotoxicity of Cit-^{4nm}Dy-CSS^{3nm} NPs

Human lung adenocarcinoma (A549) cells were seeded (75 000 cells) in a 6-well plate to a final volume of media of 1 mL. After 48 h the media was removed from wells, and fresh media containing Cit-^{4nm}Dy-CSS^{3nm} NPs (50 μg mL^{-1}, 250 μg mL^{-1}, 500 μg mL^{-1}) was added. The Cit-^{4nm}Dy-CSS^{3nm} NPs were incubated at 37 °C with the cells for 24 h. After the incubation, the cells were washed 3 times with PBS, followed by the addition of 250 μL of trypsin, diluted with 750 μL phenol red-free media and centrifuged (1000 RCF, 6 min). After the cells were decanted, 1 mL of PBS with 0.2% DMSO, 1 μM calcein-AM, and 2 μM ethidium homodimer-1 were added. The mixture was vortexed briefly three times. All cell experiments including controls were performed in triplicates. Flow cytometry (Beckman Coulter Gallios Flow Cytometer) was performed doing standard compensation and gating. The flow cytometry data analysis was performed with Kaluza software.

Conflicts of interest

There are no conflicts to declare.

Acknowledgements

References

1 X. Y. Wong, A. Sena-Torralba, R. Alvarez-Diduk, K. Muthoosamy and A. Merkoci, *ACS Nano*, 2020, **14**, 2585–2627.
2 C. Duan, L. Liang, L. Li, R. Zhang and Z. P. Xu, *J. Mater. Chem. B*, 2018, **6**, 192–209.
3 Z. Li, Y. Zhang, H. La, R. Zhu, G. El-Banna, Y. Wei and G. Han, *Nanomaterials*, 2015, **5**, 2148–2168.
4 L. Prodi, E. Rampazzo, F. Rastrelli, A. Speghini and N. Zaccheroni, *Chem. Soc. Rev.*, 2015, **44**, 4922–4952.
5 Y. Li, Y. Gu, W. Yuan, T. Cao, K. Li, S. Yang, Z. Zhou and F. Li, *ACS Appl. Mater. Interfaces*, 2016, **8**, 19208–19216.
6 F. S. Ferreira, A. J. de Morais, C. M. Santos Calado, F. Iikawa, O. D. D. Couto Junior, G. Brunet, M. Murugesu, I. O. Mazali and F. A. Sigoli, *Nanoscale*, 2021, **13**, 14723–14733.
7 C. Cressoni, F. Vurro, E. Milan, M. Muccilli, F. Mazzer, M. Gerosa, F. Boschi, A. E. Spinelli, D. Badocco, P. Pastore, N. F. Delgado, M. H. Collado, P. Marzola and A. Speghini, *ACS Appl. Mater. Interfaces*, 2023, **15**, 12171–12188.
8 Y. I. Park, K. T. Lee, Y. D. Suh and T. Hyeon, *Chem. Soc. Rev.*, 2015, **44**, 1302–1317.
9 Y. Zhang, G. K. Das, V. Vijayaragavan, Q. C. Xu, P. Padmanabhan, K. K. Bhakoo, S. T. Selvan and T. T. Tan, *Nanoscale*, 2014, **6**, 12609–12617.
10 X. Jin, F. Fang, J. Liu, C. Jiang, X. Han, Z. Song, J. Chen, G. Sun, H. Lei and L. Lu, *Nanoscale*, 2015, **7**, 15680–15688.
11 G. Chen, I. Roy, C. Yang and P. N. Prasad, *Chem. Rev.*, 2016, **116**, 2826–2885.
12 M. Raab, A. Skripka, J. Bulmahn, A. Pliss, A. Kuzmin, F. Vetrone and P. Prasad, *ACS Appl. Bio Mater.*, 2022, **5**, 4948–4954.
13 Z. Yi, Z. Luo, X. Qin, Q. Chen and X. Liu, *Acc. Chem. Res.*, 2020, **53**, 2692–2704.
14 J. Zhou, Z. Liu and F. Li, *Chem. Soc. Rev.*, 2012, **41**, 1323–1349.
15 J. Zhou, Q. Liu, W. Feng, Y. Sun and F. Li, *Chem. Rev.*, 2015, **115**, 395–465.

16 E. Hemmer, N. Venkatachalam, H. Hyodo, A. Hattori, Y. Ebina, H. Kishimoto and K. Soga, *Nanoscale*, 2013, **5**, 11339–11361.

17 A. Gnach, T. Lipinski, A. Bednarkiewicz, J. Rybka and J. A. Capobianco, *Chem. Soc. Rev.*, 2015, **44**, 1561–1584.

18 P. Verwilst, S. Park, B. Yoon and J. S. Kim, *Chem. Soc. Rev.*, 2015, **44**, 1791–1806.

19 J. Wahsner, E. M. Gale, A. Rodriguez-Rodriguez and P. Caravan, *Chem. Rev.*, 2019, **119**, 957–1057.

20 N. J. J. Johnson, W. Oakden, G. J. Stanisz, R. Scott Prosser and F. C. J. M. van Veggel, *Chem. Mater.*, 2011, **23**, 3714–3722.

21 N. Liu, R. Marin, Y. Mazouzi, G. O. Cron, A. Shuhendler and E. Hemmer, *Nanoscale*, 2019, **11**, 6794–6801.

22 H. Chen, X. Li, F. Liu, H. Zhang and Z. Wang, *Mol. Pharm.*, 2017, **14**, 3134–3141.

23 H. Zhang, Y. Wu, J. Wang, Z. Tang, Y. Ren, D. Ni, H. Gao, R. Song, T. Jin, Q. Li, W. Bu and Z. Yao, *Small*, 2018, **14**, 1702951.

24 S. Liu, J. C. Brisset, J. Hu, E. M. Haacke and Y. Ge, *J. Magn. Reson. Imaging*, 2018, **47**, 621–633.

25 S. Viswanathan, Z. Kovacs, K. N. Green, S. J. Ratnakar and A. Dean Sherry, *Chem. Rev.*, 2010, **110**, 2960.

26 J. Zhao, H. Hu, W. Liu and X. Wang, *Nanoscale Adv.*, 2021, **3**, 463–470.

27 G. K. Das, N. J. Johnson, J. Cramen, B. Blasiak, P. Latta, B. Tomanek and F. C. van Veggel, *J. Phys. Chem. Lett.*, 2012, **3**, 524–529.

28 X. Zhang, B. Blasiak, A. J. Marenco, S. Trudel, B. Tomanek and F. C. J. M. van Veggel, *Chem. Mater.*, 2016, **28**, 3060–3072.

29 A. Banerjee, B. Blasiak, A. Dash, B. Tomanek, F. C. J. M. van Veggel and S. Trudel, *Chem. Phys. Rev.*, 2022, **3**, 011304.

30 Y. Deng, H. Wang, W. Gu, S. Li, N. Xiao, C. Shao, Q. Xu and L. Ye, *J. Mater. Chem. B*, 2014, **2**, 1521–1529.

31 W. Fan, B. Shen, W. Bu, F. Chen, K. Zhao, S. Zhang, L. Zhou, W. Peng, Q. Xiao, H. Xing, J. Liu, D. Ni, Q. He and J. Shi, *J. Am. Chem. Soc.*, 2013, **135**, 6494–6503.

32 S. He, N. J. J. Johnson, V. A. Nguyen Huu, E. Cory, Y. Huang, R. L. Sah, J. V. Jokerst and A. Almutairi, *Nano Lett.*, 2017, **17**, 4873–4880.

33 S. Biju, M. Harris, L. V. Elst, M. Wolberg, C. Kirschhock and T. N. Parac-Vogt, *RSC Adv.*, 2016, **6**, 61443–61448.

34 Y. Su, L.-N. Hao, K. Liu, J. Zhang, L. Dong, Y. Xu, Y. Lu and H.-S. Qian, *RSC Adv.*, 2018, **8**, 12944–12950.

35 W. Yuan, D. Yang, Q. Su, X. Zhu, T. Cao, Y. Sun, Y. Dai, W. Feng and F. Li, *Adv. Funct. Mater.*, 2016, **26**, 8631–8642.

36 Y. Liu, K. Ai, J. Liu, Q. Yuan, Y. He and L. Lu, *Angew. Chem., Int. Ed.*, 2012, **51**, 1437–1442.

37 J. H. Hubbell and S. M. Seltzer, X-ray mass attenuation coefficients, NIST standard reference database 126, DOI: DOI: **10.18434/T4D01F**, accessed 07 June 2023.

38 K. Ai, Y. Liu, J. Liu, Q. Yuan, Y. He and L. Lu, *Adv. Mater.*, 2011, **23**, 4886–4891.

39 I. Halimi, E. M. Rodrigues, S. L. Maurizio, H.-Q. T. Sun, M. Grewal, E. M. Boase, N. Liu, R. Marin and E. Hemmer, *J. Mater. Chem. C*, 2019, **7**, 15364–15374.

40 R. Shi, C. D. S. Brites and L. D. Carlos, *Small Struct.*, 2022, **3**, 2100194.

41 S. Dühnen and M. Haase, *Chem. Mater.*, 2015, **27**, 8375–8386.

42 S. M. Kaczmarek, T. Tsuboi, M. Ito, G. Boulon and G. Leniec, *J. Phys.: Condens. Matter*, 2005, **17**, 3771–3786.

43 Q. Jin, S. Gao, Y. Xu and A. Caggiano, *Adv. Mater. Sci. Eng.*, 2021, **2021**, 1–9.

44 C. Homann, L. Krukewitt, F. Frenzel, B. Grauel, C. Wurth, U. Resch-Genger and M. Haase, *Angew. Chem., Int. Ed.*, 2018, **57**, 8765–8769.

45 R. Naccache, P. Chevallier, J. Lagueux, Y. Gossuin, S. Laurent, L. Vander Elst, C. Chilian, J. A. Capobianco and M. A. Fortin, *Adv. Healthcare Mater.*, 2013, **2**, 1478–1488.

46 C. D. S. Brites, A. Millán and L. D. Carlos, Lanthanides in Luminescent Thermometry, in *Handbook on the Physics and Chemistry of Rare Earths*, ed. J. C. G. Bunzli and V. K. Pecharsky, Elsevier Science, B. V., Amsterdam, 2016, vol. 49, p. 339.

47 Y. X. Wang, *Quant. Imaging Med. Surg.*, 2011, **1**, 35–40.

48 M. Rohrer, H. Bauer, J. Mintorovitch, M. Requardt and H. J. Weinmann, *Invest. Radiol.*, 2005, **40**, 715–724.

49 M. Harris, L. Vander Elst, S. Laurent and T. N. Parac-Vogt, *Dalton Trans.*, 2016, **45**, 4791–4801.

50 P. Caravan, M. T. Greenfield and J. W. Bulte, *Magn. Reson. Med.*, 2001, **46**, 917–922.

51 Y. Zhang, J. D. Lin, V. Vijayaragavan, K. K. Bhakoo and T. T. Tan, *Chem. Commun.*, 2012, **48**, 10322–10324.

52 S. Biju, J. Gallo, M. Banobre-Lopez, B. B. Manshian, S. J. Soenen, U. Himmelreich, L. Vander Elst and T. N. Parac-Vogt, *Chem. – Eur. J.*, 2018, **24**, 7388–7397.

53 M. Norek, E. Kampert, U. Zeitler and J. A. Peters, *J. Am. Chem. Soc.*, 2008, **130**, 5335–5340.

54 J. Yin, F. Xu, H. Qu, C. Li, S. Liu, L. Liu and Y. Shao, *Phys. Chem. Chem. Phys.*, 2019, **21**, 11883–11891.

55 E. Gianolio, E. D. Gregorio and S. Aime, *Eur. J. Inorg. Chem.*, 2019, 137–151.

56 P. L. McCormack, *Clin. Drug Invest.*, 2013, **33**, 155–166.

57 B. Johnson, J. L. Hinshaw, J. B. Robbins and P. J. Pickhardt, *AJR, Am. J. Roentgenol.*, 2016, **206**, 1202–1207.

58 T. E. Reeves, P. Mah and W. D. McDavid, *Dentomaxillofac. Radiol.*, 2012, **41**, 500–508.